Journal of ELECTRONIC MATERIALS, Vol. 49, No. 1, 2020
https://doi.org/10.1007/s11664-019-07711-8

A Study on Electrical and Electrochemical Characteristics of Friction Stir Welded Lithium-Ion Battery Tabs for Electric Vehicles

OMKAR MYPATI,[1,4] DEBASISH MISHRA,[2,5] SURYAKANTA SAHU,[2,6] SURJYA K. PAL,[1,7] and PRAKASH SRIRANGAM[3,8]

1.—Friction Stir Welding Laboratory, Department of Mechanical Engineering, Indian Institute of Technology Kharagpur, Kharagpur 721302, India. 2.—Advanced Technology Development Centre, Indian Institute of Technology Kharagpur, Kharagpur 721302, India. 3.—Warwick Manufacturing Group, University of Warwick, Coventry CV4 7AL, UK. 4.—e-mail: omkar.mypati@iitkgp.ac.in. 5.—e-mail: debsmishra02@gmail.com. 6.—e-mail: suryakanta@iitkgp.ac.in. 7.—e-mail: skpal@mech.iitkgp.ac.in. 8.—e-mail: P.Srirangam@warwick.ac.uk

This study attempts to join copper (Cu) and aluminium (Al) sheets in micro-thickness by using friction stir welding. These materials are being used as current collectors in lithium-ion (li-ion) battery which are employed as power sources for electric vehicles. Several experiments have been carried out, followed by the measurement of electrical conductivity by using a 4-probe setup and electrochemical analysis by using a potentiodynamic polarization test and an electro impedance spectroscopy test in lithium phosphorus hexafluoride (LiPF6), an electrolytic medium. The welded samples have been found to achieve an electrical conductivity of 9% less than the base Cu and the corrosion resistance of the welded samples has been found to be increasing because of the formation of inter-metallic compounds such as Al_4Cu_9, $AlCu_4$ and AlCu at the weld interface. Among them $AlCu_4$ has the highest hardness and the recovery elastic modulus than the rest.

Key words: Hybrid electric vehicles, lithium-ion battery, electrical conductivity, corrosion, friction stir welding

INTRODUCTION

With the increasing concern for reducing fuel emission and conservation of environment, hybrid electric vehicles (HEVs) have been one among the greatest technological innovations. The HEVs consist of both fuel and batteries as energy sources, and are gaining popularity as they help improve the fuel economy, thereby reducing the environmental pollution. One of the major components of the HEVs is the battery, and mostly it is made up of lithium ion (li-ion) owing to its high specific energy content.[1,2] In order to be used in a vehicle, several such batteries are connected to each other in a series fashion by means of a busbar forming a pack of batteries. Busbar refers to the inter-connectors being used in between two individual batteries in a battery pack.[3] The manufactured battery pack is intended to serve as a means of high current source to the vehicle.[4] However, in order to achieve this, materials with high thermal and electrical conductivity are desirable to be used for manufacturing this battery pack. Copper (Cu) and aluminium (Al) are two such metals which are being widely used in this area owing to their high thermal and electrical conductivity.[5,6] These two properties have rendered them being called as "electronic materials".[7] These metal sheets are required to be joined together by the available joining techniques to be used in manufacturing of the battery pack.[8] However, as

(Received May 14, 2019; accepted October 9, 2019; published online October 29, 2019)

these dissimilar metal sheets to be used in the battery pack have thickness less than 1 mm, it is very difficult to make use of the conventional welding methods to join them. The following paragraph discusses the techniques being used by researchers to join metal sheets having thickness in the micron range.

Joining of Micro-thickness Sheets

The joining of micro-size sheets can be performed by three techniques, namely soldering, brazing and welding.[8] Soldering is being used to make temporary connections between materials and mostly the technique is being used in the printed circuits boards (PCB) and joining of electronic materials.[9] This process is applicable for joining tabs to cylindrical cells but is not suitable for joining of one tab to the other.[8] The advantage with this method is its utilization in joining dissimilar materials having different melting temperatures. However, the resultant welded joint is not rigid enough to sustain any fatigue that might occur in several situations.[10] This limits the application of the technique to be utilized in joining of metal sheets for HEVs.

While Cu has a melting temperature of about 1085°C, the melting temperature of aluminium sheets is around 660°C. Thus, while applying the brazing technique to join Cu to Al is again difficult because of this huge difference in their melting temperatures. During, brazing, the heat will always be directed towards Cu. However, once the heat is transferred from Cu to Al, the Al part would start burning, resulting in fast destruction of the welded component. In a recent work, Cu and Al have been attempted to join by brazing where the base materials selected were a pure Al alloy of grade 1050 and Cu alloy of grade C1020; both the sheets having thickness of 0.8 mm.[11] Keeping in mind the difference in the melting temperatures of these two metal sheets, a third material has been utilized, i.e., being referred as a cover plate to join these Cu and Al. This cover plate is a cold rolled steel sheet having high specific resistance and low heat conductivity. Successful spot brazed joints were obtained by this strategy, and the tensile strength of the joints has been reported to be 40% more than that of the joint fabricated without any cover plate. However, during brazing, it was found that placing the cover plate on the joint line resulted in melting of the Al component. Thus, the joint was unsuccessful and the cover plate was only kept on the Cu side. Occurrence of interfacial reaction on the Al side has also been reported. Though, a welded joint between the two sheets was obtained, the usage of the cover plate for this purpose also added extra weight to the component. Thus, it can be concluded that brazing technique is also not at all a ripe solution for joining Cu and Al sheets.

Gas metal arc welding (GMAW) and gas tungsten arc welding (GTAW) are some of the examples of conventional arc welding. As discussed in the preceding paragraph, Al has a melting temperature of around 660°C. However, being an active metal, when it is exposed to air, it reacts with oxygen and forms an oxide layer on its surface. The melting temperature of this oxide layer is around three times more than that of the pure Al alloy. This oxide has higher affinity towards hydrogen which results in the formation of porosity during welding. Thus, applying GMAW to weld Al alloys is difficult. Further owing to the difference in the melting temperatures of Cu and Al alloys, solidification cracking may also occur in the weld. GMAW has been successfully utilized to weld stainless steel sheets of 0.6 mm thickness.[12] The GMAW process has also been utilized to weld dissimilar materials such as Al to steel.[13] However, it will be difficult to weld Cu and Al because of their high heat conductivity resulting in non-uniform expansion and contraction. GTAW has been widely preferred over GMAW because of features such as low current supply during the welding process and use of a non-consumable tungsten electrode instead of a constant wire feed unit.[14] However, the joint strength gets affected by the formation of brittle inter-metallic compounds (IMC).[15]

To summarize, the conventional fusion welding techniques will not be feasible to join Cu and Al with thickness in the microns range because of high thermal conductivity of these materials yielding high dissipation of heat. In addition, the fusion welding techniques make use of filler materials which leads to extra weight addition to the welded component. As the concern here is the HEVs, inclusion of components which are lighter in weight will help improve the fuel efficiency. As such, various advanced welding techniques are being explored to join these sheet metals. One such advanced welding technique is the laser beam welding which has been used to join sheets of 0.8 mm thickness by using a special laser with short pulse duration.[16] The major disadvantage associated with the laser beam welding method is that, it is not a feasible technique for materials with high reflectivity, as the radiations cannot be absorbed.[17] Both Al and Cu possess high reflectivity.

An electric vehicle is equipped with a battery pack. This pack consists of several individual cells interconnected in parallel or series pattern to achieve a desired specific energy and power.[8] When the joining of electrodes is of similar materials, it forms a parallel pattern, and when dissimilar materials are being used for joining of electrodes, they form a serial pattern. The battery pack can be assembled in two configurations i.e. cell-to-cell, and cell-to-busbar.[18] In the present study, authors have focused to join in cell-to-cell configuration, where the cathode (Al) of one cell is welded to anode (Cu) of adjacent cell. For this joining, an advanced welding technique called friction stir welding (FSW) has been utilized to overcome the problems associated

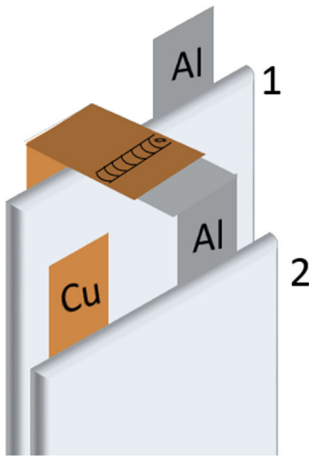

Fig. 1. Battery pack fabrication by using FSW processes.

with the fusion welding and others. This attempt is aimed at the formation of a battery pack resulting in a series connection of the cells. For better clarity, a picture depicting this cell joining is shown in Fig. 1. Two cells (1 and 2) have been joined, where the Cu of cell 1 has been joined with Al of cell 2, and so on, forming a battery pack. The Cu-Al welded joint obtained will not be utilized as a current collector or electrode, rather, it will help to form the battery pack. The Al left out, as shown in the said figure will act as cathode, and similarly, the Cu of the last cell to be connected in series, will act as anode. The following paragraph discusses FSW.

Friction Stir Welding

FSW welds materials being on their solid state only by using a non-consumable tool.[19–21] This tool is mounted in the machine spindle and is allowed to rotate. The rotating tool plunges into the job and generates frictional heat because of the rubbing action occurring between the tool surface and the job.[22] As such, the material being used to fabricate this tool has higher strength than that of the job to be welded. As the process does not involve any filler material unlike fusion welding techniques, weight of the welded component does not increase. In addition, it is free of any kind of fumes and involves no harmful gases, rendering the process to be environmentally friendly.[22] In order to deal with the difference in the melting temperatures in case of dissimilar materials, several strategies have been developed which have been discussed in the following sentences.[23,24] These strategies include shifting the tool from the joint line towards harder material, placing the base materials in lap configuration with harder material on the bottom, etc.[25,26] During welding of Al to steel sheets by using FSW, successful weld joints have been achieved by placing those sheets in a lap joint configuration.[27,28] This included placing the Al sheet over the steel sheet. Upon plunging of the tool inside these workpieces, a larger portion of pin remains inside the Al, and a smaller portion will be inside the steel part. With the generation of frictional heat and plastic deformation of the workpieces, fragments of steel particles are generated which upon the action of the rotating and translating tool, adheres into the Al matrix.[26] Since Al has got a high value of thermal conductivity, it dissipates the heat, and the steel particles get adhered resulting in the formation of a joint. Several research works have been reported which are concerned with the joining of Al and Cu by using FSW. The paragraph given below depicts research works of such cases.

The joining of pure Cu and pure Al alloy sheets in a lap joint configuration has been attempted by using a tool fabricated from tool steel.[29] The parameters such as the tool rotational speed (ω) and weld speed (v) opted for this study were 800 rpm and 50 mm/min, respectively. The thickness of the Cu sheet in this case is 1.9 mm, and that of the Al is 0.9 mm. Similarly, in another work, pure Al of grade 1100-H24 sheets of 2 mm thickness have been attempted to join with Cu sheets of 1 mm thickness.[30] In this study, the parameters selected were ω in the range of 1000–2500 rpm and v in the range of 200–300 mm/min. Very few other studies have reported the joining of Cu and Al sheets in butt joint configuration. This includes joining of oxygen-free Cu sheet with high phosphorus content and Al5083 sheet, both of 1 mm thickness by using a tool having a conical pin fabricated from tool steel.[31] The parameters in this study were ω of 750–1000 rpm and v of 160–250 mm/min. In another study, Cu sheets of grade deoxided high phosphorous DHP-R420 have been attempted to weld with Al5083-H111, both of 1 mm thickness by using a tool fabricated from tool steel.[32] The parameters in this study were ω of 750–1250 rpm and v of 160–250 mm/min. The Al-rich IMC, i.e., $CuAl_2$ initiates the slipping action under the tool shoulder and causes decrease in axial force and torque.[32] From the preceding survey on the joining of micro-thickness sheets by using FSW, it can be summarized that the parameters for this sort of welding include high values of ω and low values of v. In addition to the above, researchers have also studied the metallurgical properties of the weld and have reported about the formation of IMCs in the weld interface.[30,33,34] These IMCs include Al_4Cu_9, $CuAl_2$, $AlCu_4$ and AlCu.[30,33,34] Generally, Cu-rich IMCs are formed at above recrystallization temperature of Cu.[35] Since the Cu is a high electric and heat conductive material, the IMCs like Al_4Cu_9 and $AlCu_4$ are highly responsible for enhancing the electrical properties of welded joints. The atomic percentage of Cu in $AlCu_4$ is of 80% than Al. Due to high heat conductivity the Cu-rich IMC dissipates heat faster and tends to form a harder IMC with high value of microhardness. Al_4Cu_9 and AlCu are grey in colour and have layer type structure.[30] The ultimate tensile strength (UTS) of such dissimilar welded structure has been found depending on the

formation of IMCs at the weld interface. With micro-thickness jobs, ω has a significant importance than v.[36] It has been reported that with materials having thickness below 0.5 mm, preferable tensile strength is achieved when welded in lap joint configuration.[37]

The present study aims at joining of Cu and Al alloys, both having micro-thickness by using FSW. The major challenge is to avoid occurrence of the sub-micron sized voids known as "Kirkendall voids". These defects are mostly found in the intermetallic zone and they have been often reported by researchers in case of joining of the electronic materials.[38] Generally, the voids formed due to Kirkendall effect are called Kirkendall voids. Since, high values of ω in the welded samples tends to cause diffusion at the interface, it thus promotes formation of Kirkendall voids.[39] With increase in temperature, there is an increase in rapid diffusion of Al in Cu in solid solution.[40] The mechanism of voids formation is due to rapid diffusion, shrinkage and linear expansion. Al diffuses in Cu, causing a stress generation in the diffusion zone. The stress experience at the Al side and the Cu side are tensile and compressive in nature, respectively.[41] The rapid diffusion of Al causes voids in the Al substrate and shrinkage in Cu due to compressive stress causing plastic flow.

Several experiments have been performed to obtain a high quality joint in between Cu and Al. Later, the welded joints have been analyzed for electrical conductivity and corrosion tests. Once, the base Cu and Al get welded, there will be formation of IMC at the weld interface owing to the dissimilar combination. These IMCs may affect the electrical conductivity of the base Cu and Al. As the welded sample is intended to be used in the battery pack of HEV which will act as the current source, it is thus essential to identify the electrical conductivity of the sample. Further, the li-ion battery has lithium phosphorus hexafluoride (LiPF6), acting as the electrolytic medium and the tab, i.e., manufactured of Cu and Al will remain inside this medium. The prolonged stay of the tab inside this electrolytic medium will cause corrosion which will ultimately affect the weld quality. Thus, it is also essential to analyze the corrosion behaviour of the welded samples.

MATERIALS AND METHODOLOGY

The 0.3 mm thick Cu sheets and 0.2 mm thick Al sheets have been selected as the base materials. These sheets were cut into a dimension of 35 mm × 70 mm (length × width). Lap joints have been fabricated where Cu sheets were placed over the Al with an over-lapping distance of 15 mm. A 6-axis, computer numeric controlled (CNC), friction stir welding machine (BISS, SP02-05-10) has been utilized to fabricate the joints. The machine has the following configurations: (1) maximum load capacity of 35 kN, (2) maximum ω of 4000 rpm, (3) v of 2500 mm/min, and (4) tilt angle (α) of ± 10°. A picture of this machine is depicted in Fig. 2. As the sheets being used in this study have micro-thickness, a special fixture has been fabricated to hold them. The picture of this fixture is depicted in Fig. 2. The tool utilized for fabricating the joints has been fabricated from H13 tool steel. The dimension of the tool has been shown diagrammatically in Fig. 3. Table I lists the process parameters used for joining the materials. As the selected base materials (Cu and Al) have high thermal conductivity, a combination of the high value of ω and low value of v has been selected to achieve a sufficient amount of heat generation and plastic deformation of the workpieces.

Post-welding, the welded samples were subjected to various tests to measure and investigate on the electrical and electro-chemical properties. This first is a 4-probe test which has been conducted to measure the electrical conductivity. The test set-up is shown in Fig. 4. The arrangement consists of four thin tungsten wires collinearly positioned and connected with probes. These probes maintain equal space among them and are placed over the sample being analyzed. The other components in this test arrangement include a constant current supply source and a nano-voltmeter. The outer probes are passed with a direct current (DC) (I) in between through the weld sample by using the constant current supply source, and the inner two probes measures in between voltage drop (V).[42–44]

A scanning electron microscope (SEM) was utilized to analyze the interface layer of the welded samples (Zeiss, EVO 60). Prior to this analysis, the samples were polished by emery papers of various grit sizes. Energy dispersive spectroscopy (EDS) was utilized next to identify the elemental composition of the weld interface. The formation of IMCs in the weld region was investigated by x-ray diffraction test (PANalytical B.V, 7602 EA). A Cu anode was used to capture the IMCs from a range of 20°–120°. The current for the same was maintained at 40 mA and the voltage at 40 kV. For determining the hardness of the IMCs, nanoindentation technique was utilized (Anton Paar, NHT). After these metallurgical analyses, the welded samples were also tested in a li-ion battery electrolyte ($LiPF_6$) medium for analyzing the corrosion of the welded samples. The parameter for potentio-dynamic polarization (PDP) was selected out from − 1 V to +1 V after reaching the open circuit potential (OCP) and data points were collected at a scanning rate of 1 mV/s. The electro-chemical impedance spectroscopy (EIS) test was carried out at 0.01 Hz to 100 kHz, and the capacitive nature and polarization resistance of the samples were determined. The test was carried out by using a potentiostat setup (Bio-Logic, SP-150), the schematic of the test is shown in Fig. 5. Afterwards, the SEM images of the samples were captured on the Cu surface. The chemical composition of the corroded samples has been measured by using EDS analysis, and the gun for the same is attached in SEM.

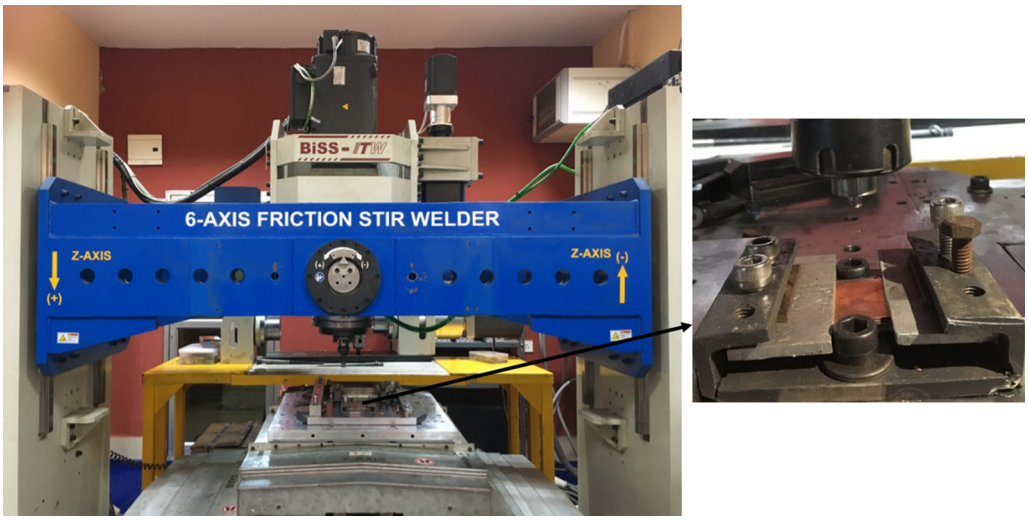

Fig. 2. Picture of FSW machine, and fabricated fixture.

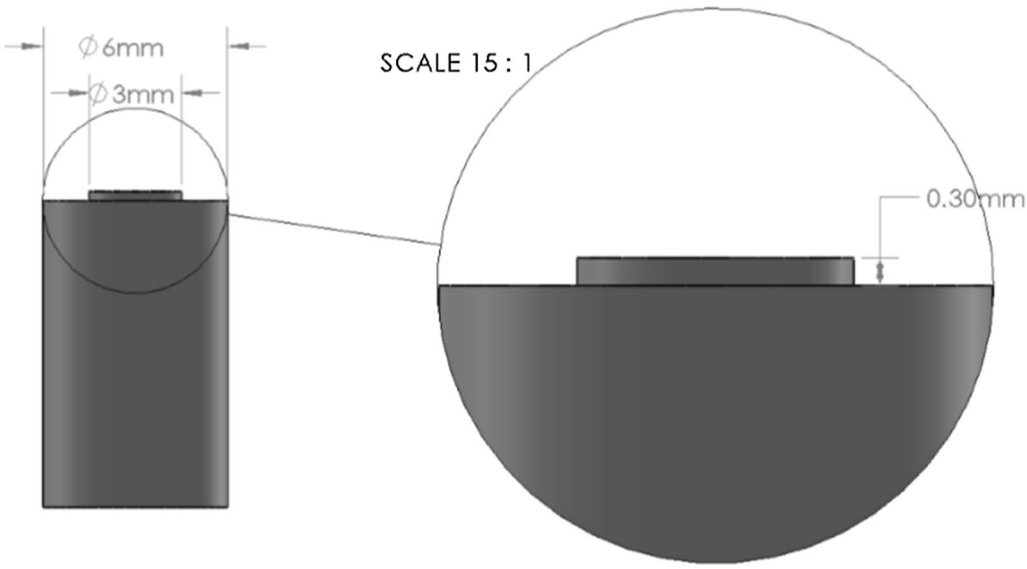

Fig. 3. Tool dimensions.

Table I. Parameters for joint fabrication

Range of parameters	Sample nomenclature		
	S_1	S_2	S_3
ω (rpm)	2500	3000	3000
v (mm/min)	50	50	60
Plunge depth (mm)		0.1	
Dwell time (s)		5	

RESULT AND DISCUSSION

Visual Inspection of the Welded Samples

Table II shows the welded samples fabricated with the employed process parameters. The sample marker as "S_2" is a defective weld with voids and rough surface appearance. This is because of the increase in ω which resulted in higher heat as compared to the condition prevailing in case of "S_1". Further, during "S_3" sample, the selected v was more as compared to "S_2" resulting in lesser heat condition and better weld quality than "S_2".

Force and Torque Variation

In order to obtain a sound weld joint for the battery tabs, it is essential to maintain a constant Z-load and minimum temperature during welding. The Z-load and torque experienced during the welding by the FSW tool is shown in Fig. 6a. The region 1 indicates the start of plunging of the rotating tool into the base materials to be welded.

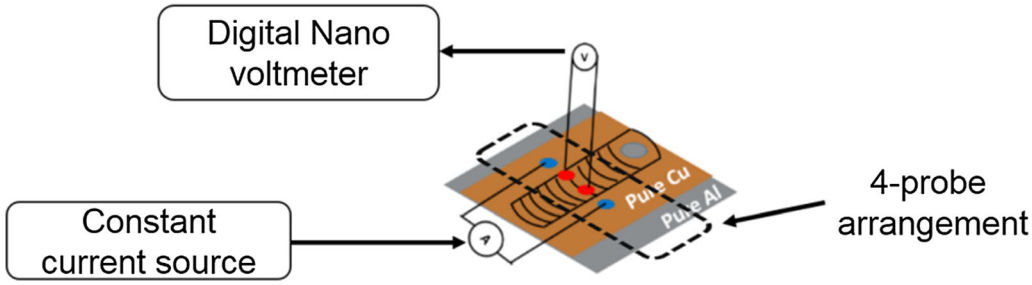

Fig. 4. High temperature resistivity setup to measure electrical conductivity.

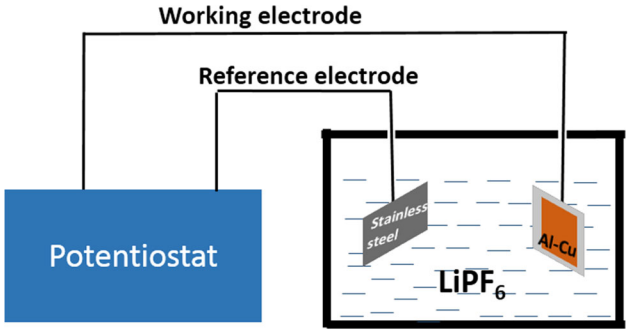

Fig. 5. Schematic diagram for corrosion test in $LiPF_6$ medium.

After the plunging, the next stage is referred as dwelling where the tool is allowed to rotate at the same position in order to conduct the heat. Here, the axial load decreases, which has been marked as region 2. This is followed by the traverse of the tool where it can be observed that the axial load again rises and remains constant during the welding. This has been referred as region 3. At last, the tool ejects out of the workpieces and the axial load decreases. A similar kind of trend can also be seen for the variation of torque with time during welding. The high peak value in case of spindle torque (marked as region 4) is due to start of the spindle motor.

The variation of average axial load with respect to time for the three welded samplesis shown in Fig. 6b. This load can be found more for S_1 because of the involvement of lower value of ω as compared to other two welded samples. With increasing ω, generation of frictional heat increases resulting in reduction of Z-load. Figure 6c shows the variation of the spindle torque in case of the three welded samples.

Study on Electrical Conductivity

The formation of void during FSW of dissimilar materials is majorly because of the differences in the inter-diffusion rates of the two materials leading to varying microstructures. In the case of Cu and Al, as the rise in temperature, the diffusion of Cu into Al also increases. This phenomenon can be depicted as per Eq. 1.[45]

$$D(T) = D_0 e^{\left(\frac{-E_{act}}{K_B T}\right)}, \tag{1}$$

where D, K_B, T and E_{act} are the diffusion coefficient, Boltzmann constant, temperature, and activation energy, respectively.

As per Eq. 1, the rate of diffusion Cu into Al increases, which leads to the formation of thick IMC layer, which can be determined by Eq. 2 depicted below.[45]

$$d(t) = \sqrt{2Dt}, \tag{2}$$

where d refers to the IMC layer thickness and t is time.

With the initiation of the flow of electrons across the weld joint, the resistance increases. This increase in resistance is due to the voids present in the weld sample which affects both electrical and thermal conditions of the sample. This also brings temperature variations in the weld zone. As a consequence, high residual stresses will develop which probably will lead to distortion and fracture.

Thus, in order to justify the application in the HEVs, investigation on the electric properties like electrical resistance and conductivity of the current collectors fabricated by FSW was essential. The ability to transfer DC along a sample is defined as electrical conductivity. The use of a 4-probe test to measure the electrical conductivity has already been highlighted in the earlier section. By using values of voltage and current obtained from the test, the measured resistivity ρ_0 can be calculated as per Eq. 3.[42,43]

$$\rho_0 = \frac{V}{I} \times 2\pi s, \tag{3}$$

where s is the probe spacing distance, which is a constant value, i.e,. 2 mm in the present set-up. However, the value obtained from Eq. 3 depends upon the width of the sample being measured and spacing of the probes. In order to obtain the true value, a correction factor $G_7\left(\frac{w}{s}\right)$ is considered, and the same has depicted in Eq. 4.[42,43]

$$G_7\left(\frac{w}{s}\right) = 2 \times \frac{\log 2}{\left(\frac{w}{s}\right)}, \tag{4}$$

where w is the width of the sample (i.e. 0.5 mm) (total width = thickness of Cu and Al, i.e. 0.3 + 0.2 mm), and s is 2 mm. Hence, as per Eq. 4,

Table II. Surface morphology of welded samples

S_1	S_2	S_3
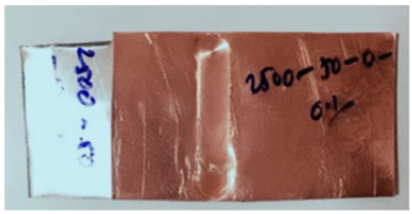	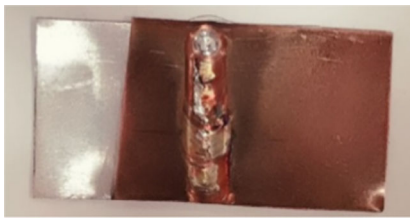	

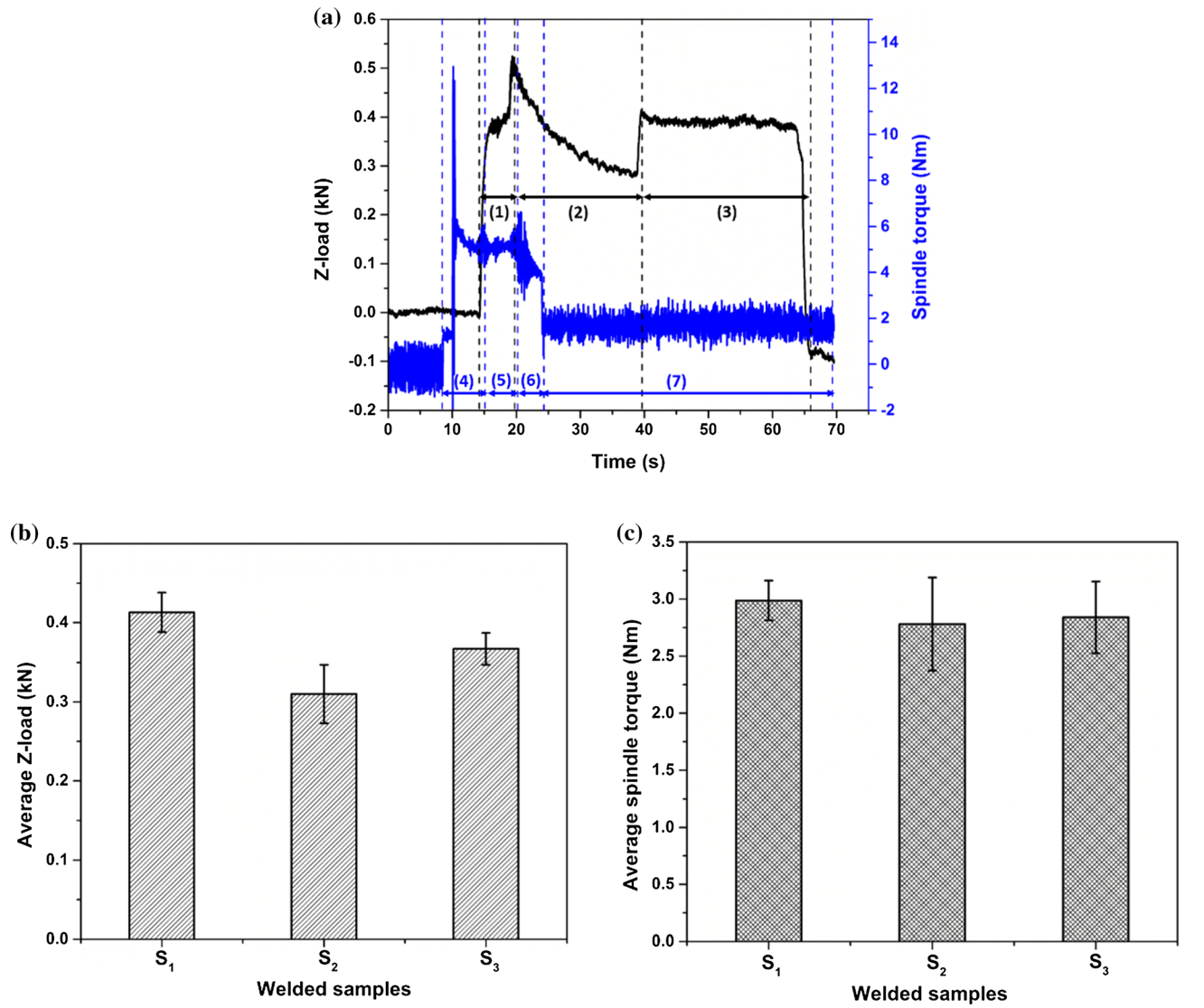

Fig. 6. (a) Variation of *Z*-load and spindle torque in S_3 welded sample, (b) average *Z*-load, and (c) average spindle torque in all welded sample.

the value of the correction factor comes to be 6.931.[42] The final value of resistivity ρ can be determined from Eq. 5.[42]

$$\rho = \frac{\rho_0}{G_7\left(\frac{w}{s}\right)}. \quad (5)$$

As stated above, the samples were analyzed in the test set-up to identify the voltage drop with respect to increasing values of current. From this, the measured resistivity value has been obtained, and the final resistivity value has been determined by applying the correction factor.

Before analyzing the welded samples, the base materials, i.e., Cu and Al were tested in the test set-up. The results (V–I plot) obtained for the base materials is plotted in Fig. 7. A linear relation can be seen existing between current and voltage from the plot. The resistance of the material is determined by slope of the plot, and the obtained results are listed in Table III. The Cu was observed to have low voltage drop as compared to Al, which indicates low resistance to the flow of electric charge, indicating higher electrical conductivity of Cu, as compared to Al. Similarly, the voltage drop across the welded samples has also been measured by passing different values of current. The results are shown in the same plot depicted in Fig. 7. It can be observed from the same figure that the values obtained for the welded samples are very close to that of the values obtained for Cu. Further, it can also be noticed that the weld samples S_1 and S_3 have a similar trend as found for Cu base material, while S_2 exhibits a little different nature. The probable reason for this could be due to the voids which have been found in case of S_2 welded sample.[46]

It can be found that S_1 has 9% value of resistance more than the base Cu, whereas S_2 and S_3 have 19% and 16% more, respectively. The probable reason for this could be the material mixing which affects these values. In order to investigate this concern, micrographs of the weld samples have been obtained by using SEM.

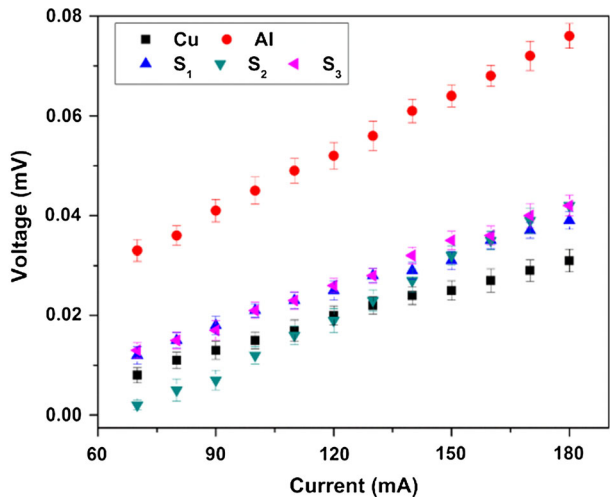

Fig. 7. V–I plot of the base materials (Cu and Al) and welded samples (S_1, S_2, and S_3).

Micrograph Analysis

The micrographs of the welded samples are depicted in Fig. 8. While the micrograph of S_1 shows a uniform weld interface, whereas both S_2 and S_3 contain voids. The S_2 welded sample has several welding defects, and in few portions, it can be seen that the Cu has detached from the Al surface in the weld interface. The micrograph shown in Fig. 8b shows improper material mixing which might probably be because of the lower electrical conductivity. Similarly, the micrograph shown in Fig. 8c, i.e., of S_3, Kirkendall voids can be seen in the joint interface because of the high rate of diffusion of Cu into the Al matrix. This diffusion phenomenon is because of high values of ω.

Further, for the higher value of electrical conductivity obtained in case of S_1 it has been attempted to be explained by means of XRD analysis. Since, S_2 has several weld defects, the XRD analysis has not been carried out for this welded sample. Figure 9 depicts the XRD plots of S_1 and S_3. In case of S_1, IMCs like Al_4Cu_9 and $AlCu_4$ have been formed whereas Al_4Cu_9 and AlCu have formed in S_3 as shown in Fig. 9a and b, respectively. As stated in the earlier sections, $AlCu_4$ is a Cu-rich IMC and is more conductive, its presence in S_1 is the probable reason behind its higher electrical conductivity than S_3.[47]

Corrosion Analysis

To analyze the corrosion behaviour of the welded samples, two different tests have been carried out namely, PDP and EIS. The following subsections explain the justification of carrying out these two tests and the obtained results.

Potentiodynamic Polarization Test

The PDP tests have been carried out in an acidic salt medium ($LiPF_6$) to measure the corrosion rate and kinetics of anode and cathode reactions occurring in case of the base materials and the welded samples.[48,49] The electrochemical parameters such as potential (E_{Corr}), corrosion current density (I_{Corr}), slope of anode and cathode (β_a) and (β_c) respectively, have been measured along with the polarization resistance (R_p) of the base materials and welded samples. All these obtained values are listed in Table IV. The values of R_p have been measured by using Eq. 6.[48]

$$R_p = \frac{\beta_c \times \beta_a}{2.3 I_{Corr} \times (\beta_c + \beta_a)} \quad (6)$$

Table III. Resistance and the electric conductivity values of the material

Materials	Electrical resistance (ohms; Ω)	At 25°C electrical conductivity (S/m)
Base metals		
Cu	2.04×10^{-4}	5.88×10^{7}
Al	3.56×10^{-4}	3.37×10^{7}
Welded samples		
S_1	2.44×10^{-4}	4.91×10^{7}
S_2	2.99×10^{-4}	4.01×10^{7}
S_3	2.82×10^{-4}	4.25×10^{7}

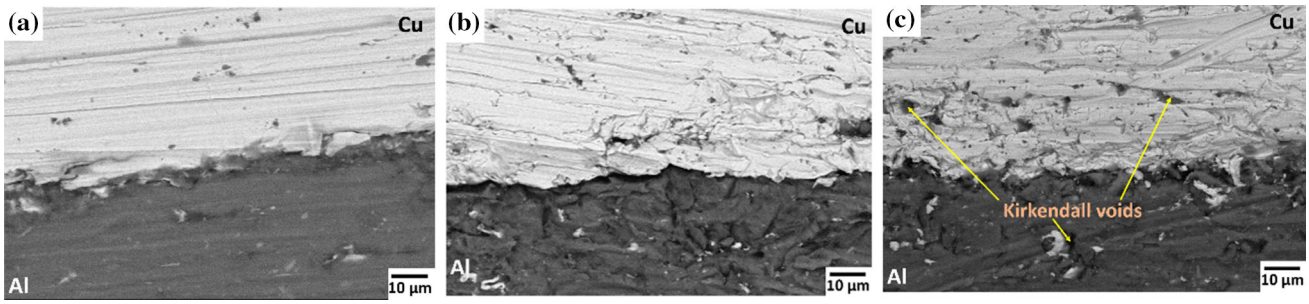

Fig. 8. SEM images at the interface of welded samples (a) S_1, (b) S_2, (c) S_3.

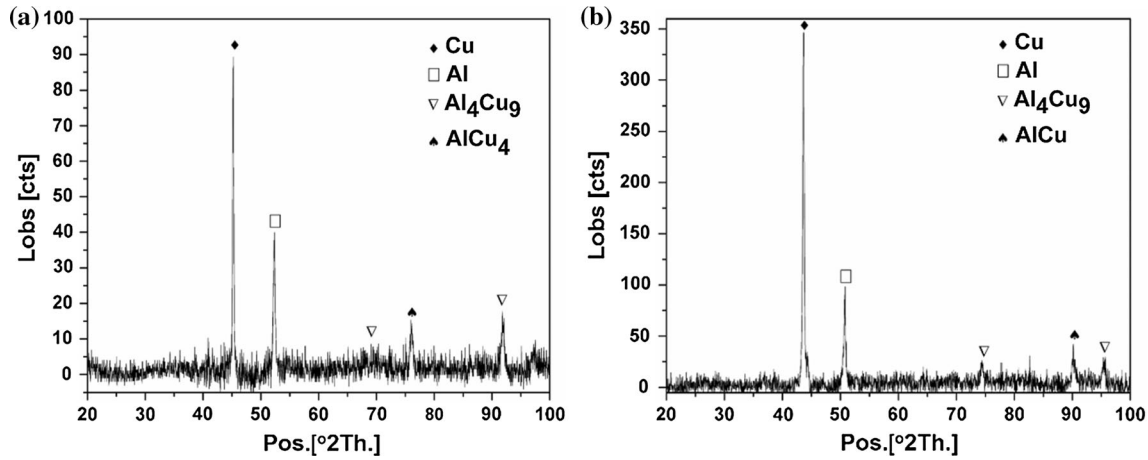

Fig. 9. XRD plots of welded samples (a) S_1 and (b) S_3.

Table IV. PDP test results for base material and welded samples in $LiPF_6$ electrolyte

Samples	E_{Corr} (mV)	I_{Corr} (μA)	β_a (mV)	β_c (mV)	R_p (Ω)	CR (mm/min)
Base metal						
Cu	313.03	1.979	280.8	161.5	22.5×10^{3}	4.1×10^{-8}
Al	− 330.22	0.328	158.7	110.5	86.3×10^{3}	2.8×10^{-8}
Welded samples						
S_1	48.90	0.711	459.8	440.0	13.7×10^{4}	5.5×10^{-9}
S_2	349.41	1.623	331.5	162.4	29.2×10^{3}	2.5×10^{-8}
S_3	− 50.97	0.447	297.5	288.9	14.2×10^{4}	6.1×10^{-9}

Usually, the cathodic reaction is considered equal to the anodic reaction and is mentioned as E_{Corr} at the equilibrium state. The E_{Corr} defines the corrosive behaviour, and as it approaches to zero, it exhibits noble behaviour. However, the negative and positive values of E_{Corr} indicated cathodic and anodic corrosion behaviour, respectively. For this study, the Tafel plots for the samples have been

shown in Fig. 10. It can be noticed from the plot that Cu has a positive E_{Corr} value. This indicates that Cu is exhibiting an anodic corrosion phenomenon. Thus, it will attract the electrons resulting in higher corrosion. However, Al has a negative E_{Corr} value indicating cathodic corrosion phenomenon. Similarly, the E_{Corr} values for S_1 and S_3 can be found near to the noble behaviour as stated above. However, in case of S_2, it is nearly seven times higher than that of S_1.

Further, in order to validate the obtained results stated above, the micrographs of these tested samples were captured by using SEM. Those captured images have been depicted in Fig. 11. Figure 11a represents the micrograph of the base Cu metal where large numbers of pits can be found. This indicates the possibility of higher corrosion. Similarly, in case of Al, the micrograph can be seen having few numbers of pits as compared to Cu. Among the welded samples, the pitting formation can be found to be more in case of sample S_2 as compared to S_1 and S_3. As ω increases, heat generation also increases; and there is a chance of formation of IMCs, which affects the corrosion behaviour.

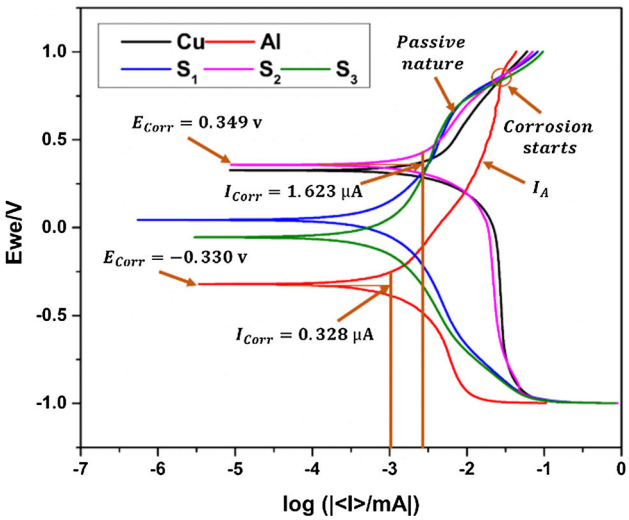

Fig. 10. PDP curves for base material and welded samples.

The variation in the slope of the anodic current (I_A), as depicted in Fig. 10 indicates the start of corrosion, whereas when there is no variation in the slope, it indicates passivation. The Al sample has less variation in slope of I_A whereas Cu has sudden change in the slope, which indicates the passive nature of Al base metal and corrosive nature for Cu base sample. The passive nature of Al is because of the formation of the oxide layer. Further, the passive nature of the welded sample S_1 is higher than S_2 which depicts high tendency to restrict the corrosion in case of S_1.

The corrosion rate (CR) can be determined by the intersection of cathodic and anodic Tafel slopes.[50] The intersection point is defined as I_{Corr}. From Eq. 6, it can be observed that I_{Corr} is inversely proportional to R_p. Thus, CR is directly proportional to I_{Corr}, equivalent weight (EW) of the sample and is inversely proportional to density (d) of the sample, and sample area exposed to the medium (A). The formulae for CR is depicted in Eq. 7.[51] The obtained values for the base metals and the welded samples are listed in Table IV.

$$CR = \frac{I_{Corr} \times k \times EW}{d \times A}, \tag{7}$$

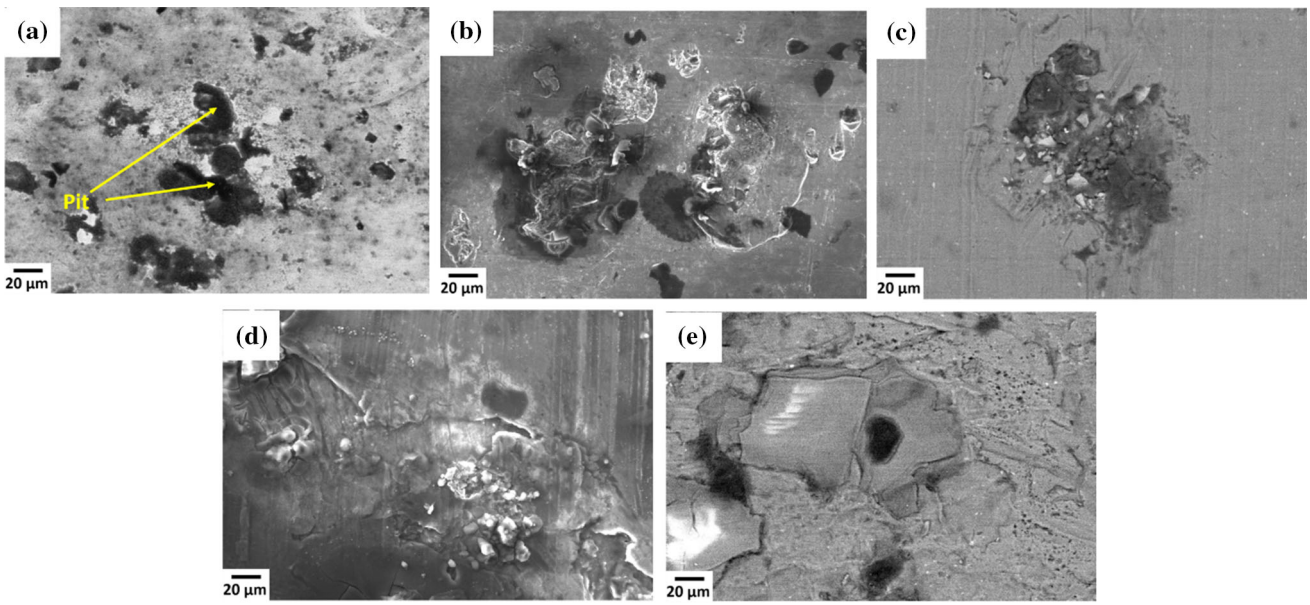

Fig. 11. SEM images of corrosion samples, (a) base Cu, (b) base Al, (c) S_1, (d) S_2, and (e) S_3.

Table V. Chemical reactions during PDP test

(a)	$xLiPF_6 \rightarrow xLiF + xPF_5$
(b)	$PF_5 + H_2O \rightarrow 2HF + PF_3O$
(c)	$Cu + PF_3O \rightarrow CuO + PF_3$
(d)	$CuO + 2HF \rightarrow CuF_2 + H_2O$
(e)	$Al_2O_3 + 2HF \rightarrow 2AlOF + H_2O$
	$2AlOF + 2HF \rightarrow Al_2OF_4 + H_2O$

where k is a corrosion rate unit constant.

The chemical reactions occurring during the PDP test are as follows (Table V):

(a) Spontaneous decomposition of $LiPF_6$ into lithium fluoride (LiF) and phosphorus pentaflouride (PF_5).
(b) Unstable PF_5 forms hydrogen fluoride (HF) and phosphoryl fluoride (PF_3O) by reacting with water. LiF forms HF and lithium oxide (Li_2O) by reacting with water.
(c) Formation of oxide layer like copper oxide (CuO) and aluminium oxide (Al_2O_3) on exposure of base metals to electrolytic medium.
(d) CuO reacts with HF to form copper (II) fluoride (CuF_2).
(e) Al_2O_3 undergoes various spontaneous reactions with HF resulting in formation of aluminium triflouride (AlF_3).

The presence of F in HF initiates the pitting corrosion in Cu as depicted in Table V (d) above. At anode, the acid HF causes metal dissolution due to autocatalysis.[48] LiF is a neutral compound consisting of combination of salts of strong acids and strong bases, and does not participate in initiation of pitting corrosion. In order to validate this mechanism, EDS analysis has been performed on the corroded sample (S_1). The pictures of the analysis are depicted in Fig. 12, where (a) shows the picture of the corroded sample; (b) shows the mapping of all the elements; (c) shows the mapping of F; (d) shows the mapping of Cu; (e) shows the mapping of P.

An interesting result observed in this study is that few particles were found accumulated over Al during the PDP test; the picture of the same has been shown in Fig. 13. These particles have been identified as Cu rich compounds. This reveals the digging of Cu particles from Cu surface which got accumulated over Al in the electrolytic medium.

Electrochemical Impedance Spectroscopy (EIS)

The corrosion behaviour of the welded samples has been studied by immersing them in an electrolytic medium which resulted in the formation of oxide layer over the metal surface. This layer acts as a protective layer and restricts the occurrence of corrosion. As such, the EIS analysis has been performed to evaluate the relative comparison of this protective layer. The Nyquist and Bode plots have been drawn from the results obtained by using EC LAB software (Biologic, V10.40,). The slope of the Nyquist curve implies the ion transfer resistance. As the slope of the curve increases, the resistance also increases, which reveals a low tendency to corrode under electrolytic medium.[52] The results are shown in Fig. 14a. The slope of Cu is less than the slope of Al, which indicates less tendency of Cu to resist the corrosion in the tested medium.

The welded samples can be seen having a lower corrosion rate than the base materials. The Nyquist plots were simulated (Z-fit) in the software, and the equivalent circuit was identified which is shown in Fig. 14a. The arcs appearing in the Fig. 14a are the part of Nyquist semicircle where their centre lies on the real part of the impedance axis. Based on this, the capacitive elements were removed and a constant phase element (Q_1) was used in the circuit.[52] The circuit was divided into four regions where, region 1 refers to the flow of charge through the electrolyte to reach the electrode. The restriction of flow of the charge is referred as electrolytic resistance (R_1). The region 2 has two circuit elements namely Q_1 and R_2. The former is a constant phase element proportional to the capacitance of the oxide layer (C_1) i.e., the charge holding capacity. The latter refers to the resistance to the flow of charge through this oxide layer. The region 3 refers to the interface of the samples with the capacitance of the interface being referred as C_3, and R_3 is the measure of corrosion resistance which can be correlated with I_{Corr}. The flow of charge occurs from oxide layer to region 3. Lastly, the region 4 refers to the substrate. The C_1 can be calculated by using Eq. 8 which depends on Q_1, R_1, and R_2.[51] The equivalent circuit elements are calculated during the Z-fit simulation, as shown in Table VI.

$$C_1 = Q_1^{\frac{1}{a_1}} \times \left\{ \frac{1}{R_1} + \frac{1}{R_2} \right\}^{\frac{(a_1-1)}{a_1}}, \tag{8}$$

where a_1 is a constant value.

The phase angle and impedance values at different frequenciesare shown in Fig. 14b and c. The negative phase angle indicates a RC circuit and the positive phase angle indicates a RL circuit. From Fig. 14b, the area under the Bode phase plot gives the charge holding capacity or capacitance since the peak values are formed towards negative phase at both lower and higher frequencies. The slope 1 as depicted in Fig. 14b is lesser than the slope 2, which indicates that Al_2O_3 is more resistive to corrosion than CuO. In Fig. 14b, at lower frequency, the slope 4 is greater than slope 3, which indicates higher resistance of Al to corrosion than Cu. Al has higher charge holding capacitance than Cu; whereas

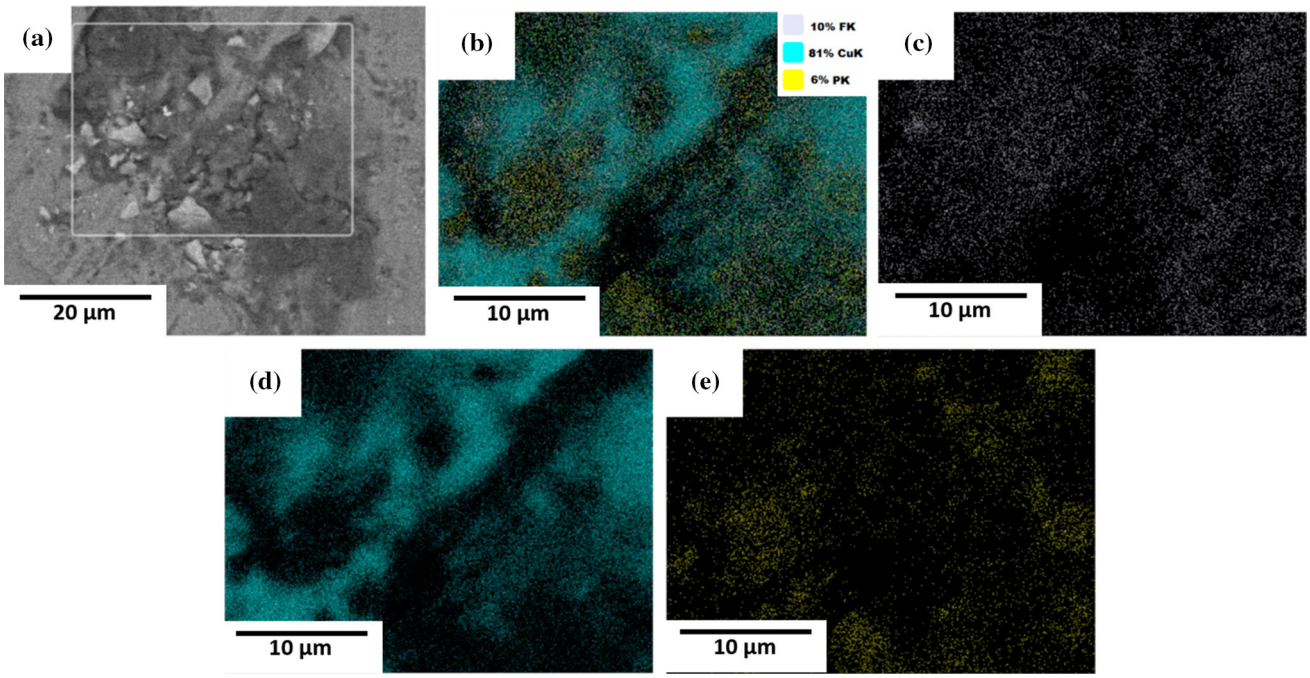

Fig. 12. EDS analysis for S_1, (a) micrograph, (b) mapping of all elements, (c) F mapping, (d) Cu mapping, and (e) P mapping.

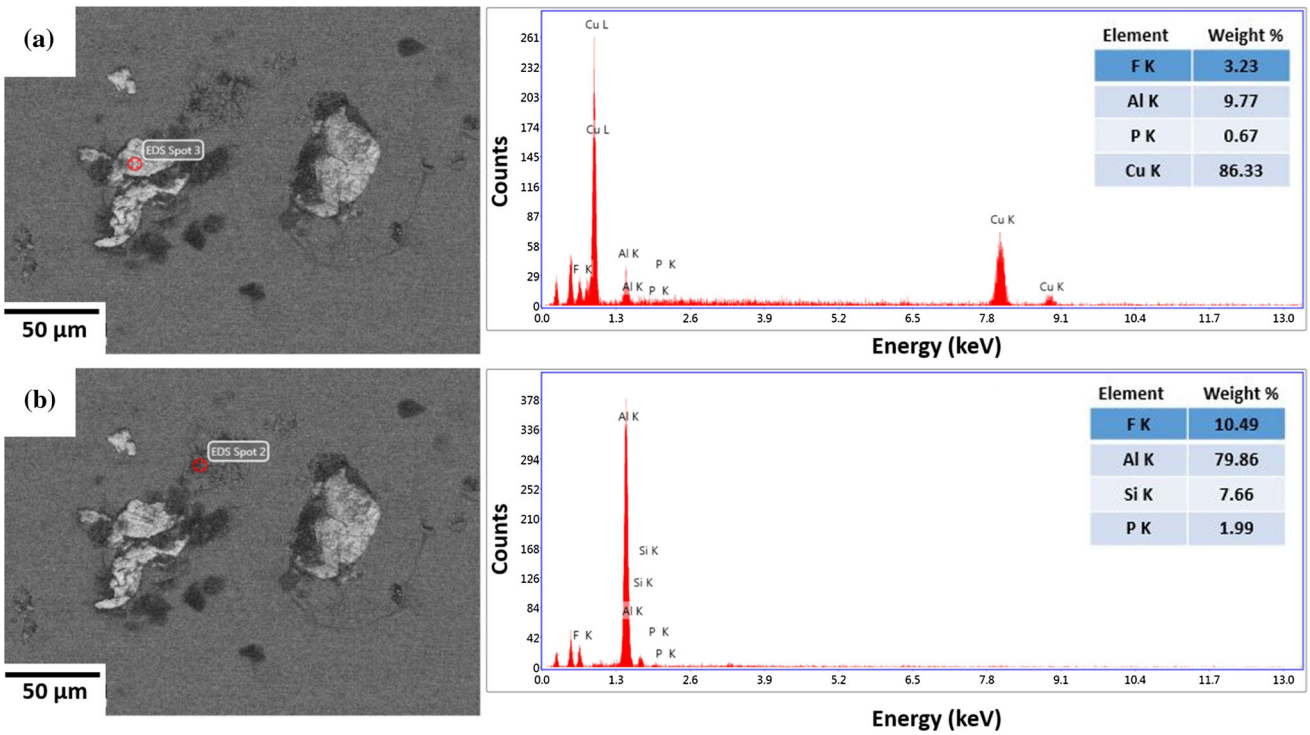

Fig. 13. EDS point analysis of S_1 at (a) over Cu, and (b) over Al.

among the welded samples, S_3 has more charge holding capacity than S_1 and S_2. The welded sample S_3 has high corrosion resistance. Further, from Fig. 14c, at low frequency, all the welded samples and Al can be found to have higher impedance value than Cu, which implies that Cu has inferior corrosion resistance with respect to the welded samples and Al base metal. At higher frequencies, sample S_3 has higher impedance and have superior corrosion resistance.

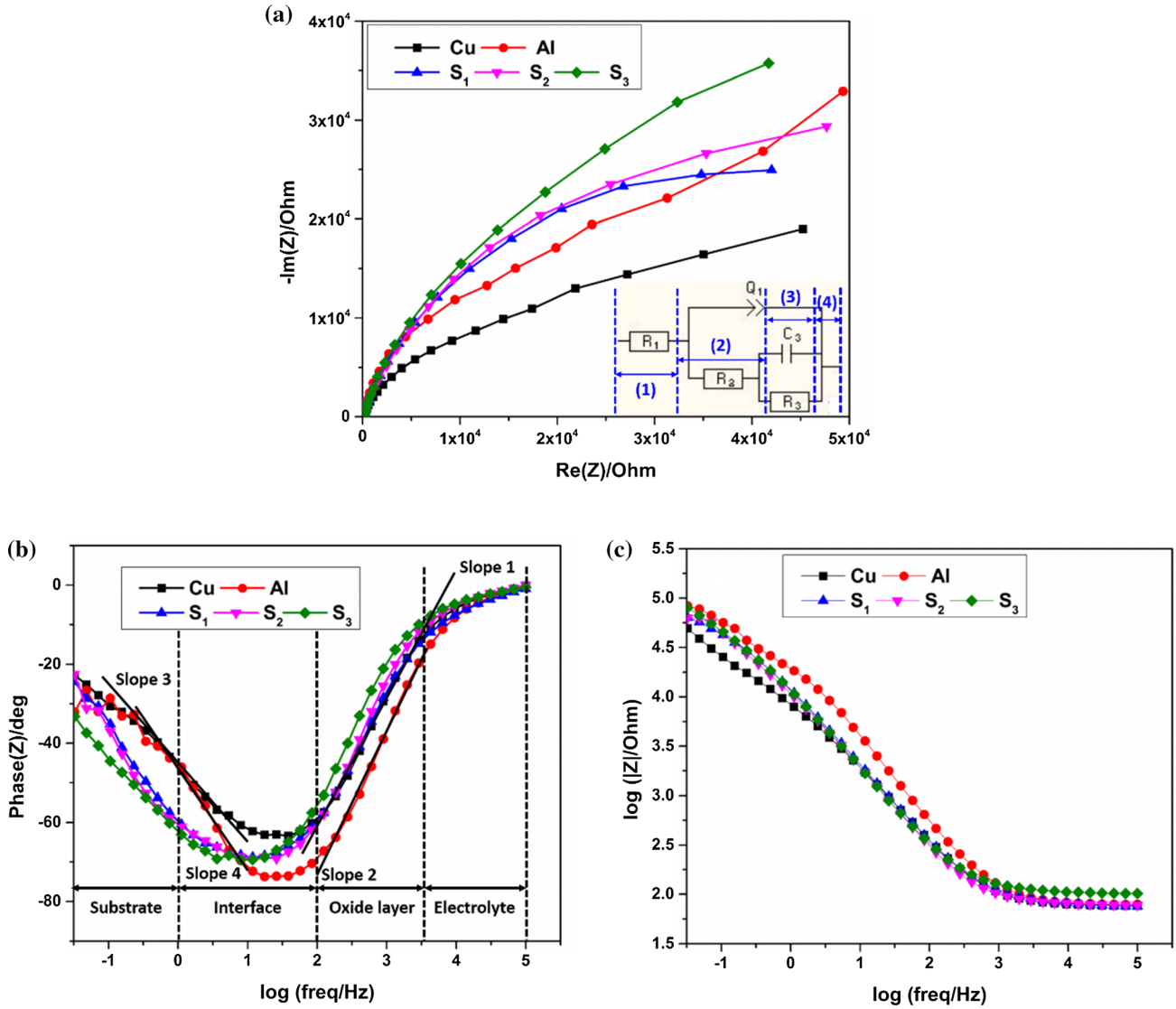

Fig. 14. EIS result, (a) Nyquist, (b) and (c) Bode plots of the welded samples at room temperature.

Table VI. Quantitative values extracted from the equivalent electrical circuit

	Parameters						
Materials	R_1 (Ω)	Q_1 (F s^(a − 1))	a_1	C_2 (μF)	R_2 (Ω)	R_3 (Ω)	C_3 (μF)
Cu	60.05	54.45×10^{-4}	0.601	1.07	290.6	53.455	1.014
Al	74.85	15.26×10^{-6}	0.76	1.36	53.176	73.93	0.985
S_1	75.64	24.42×10^{-6}	0.747	2.27	72.905	14.24	0.130
S_2	75.31	31.18×10^{-6}	0.724	2.42	79.835	18.46	0.303
S_3	81.49	18.93×10^{-6}	0.775	2.38	86.60	10.665	0.202

Nanoindentation

The mechanical characterization of IMCs has been performed by using nanoindentation test with a constant load of 10 mN and 10 s indentation time. Figure 15 depicts the load versus displacement curve, and micrographs of the indent point. The loading curves depicts the Young's modulus (E), where the unloading curves provide hardness, contact area and percentage of elastic recovery (R) of the sample being measured.[53] R during unloading

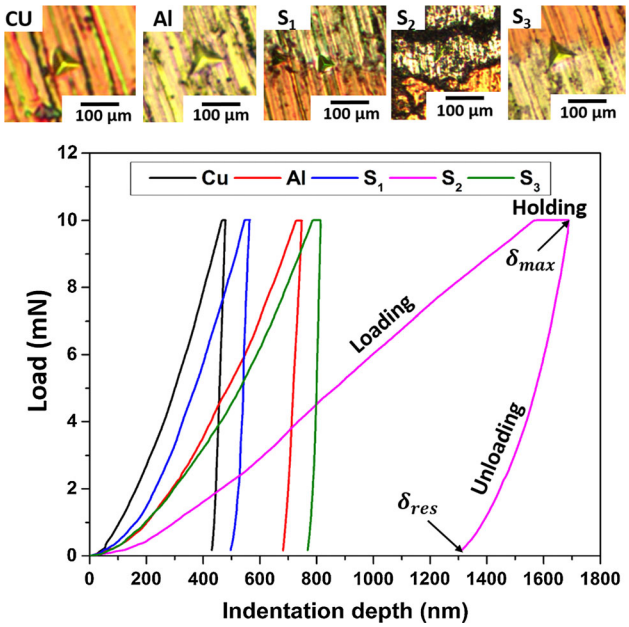

Fig. 15. Nanoindentation of the base and welded samples with micrographs of indent.

Table VII. Mechanical properties of the samples

Samples	Properties	
	***E* (GPa)**	***R* (%)**
Cu	95.62	10.07
Al	42.42	8.77
S_1	75.02	11.65
S_2	5.82	22
S_3	56.38	5.53

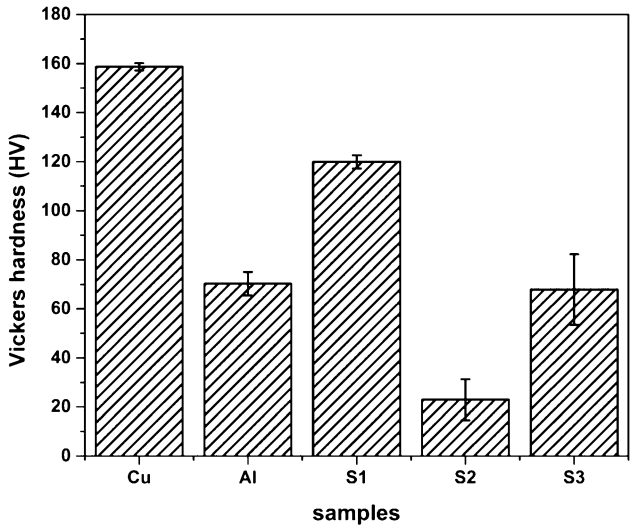

Fig. 16. Hardness of the base and welded samples at the weld interface.

can be measured by using Eq. 9,[53] and the results obtained in this study are shown in Table VII.

$$R = \frac{\delta_{\max} - \delta_{\text{res}}}{\delta_{\max}} \times 100, \quad (9)$$

where $\delta_{\max}$ is maximum displacement and δ_{res} is the residual displacement

Cu has higher resistance to deformation than Al. During the loading condition, it was observed that the slope of the curve for Cu is less than Al indicating the occurrence of plastic deformation of the metal. On the other hand, both elastic and plastic deformations have been observed for Al. The IMCs present in the welded sample S_1 are Cu-rich (i.e., Al_4Cu_9 and $AlCu_4$) which depicts a similar trend as obtained for Cu in case of loading and unloading conditions. Sample S_3 has a similar trend for these curves as found for Al. However, sample S_2 has a higher slope, which indicates the occurrence of elastic deformation. This is because of the presence of voids in the weld sample which have been occupied by resins, as depicted in Fig. 15. The welded sample S_1 has high value of E which indicates that it has high stiffness. Due to uneven mixing and presence of voids in sample S_2, E is very low and R is very high. The IMCs $AlCu_4$ have higher E and R than AlCu.

Further, the indent point size of Cu is less than Al because of its high value of hardness. The results have been depicted in Fig. 15. Similarly, S_1 has small indent point than S_3 which again indicates that $AlCu_4$ is harder than AlCu due to the presence of rich Cu.

Researchers have reported that the hardness can be correlated with corrosion resistance.[54] The hardness increases with increase in corrosion resistance which is because of the reduction in grain size during the welding processes. Similar results have also been observed in the present study. The weld sample S_1 has higher corrosion resistance than S_3, where it can be observed that hardness of the sample S_1 is higher than the S_3 result have been depicted in Fig. 16.

CONCLUSION

The current study is concerned with the fabrication of *electronic materials* by using FSW to be used in the battery pack of EVs. The potential of joining microthickness materials by using FSW has been achieved and the automobiles industries can utilise this process prior to other welding techniques for joining of cell to cell and cell to busbar. It has been found that at higher ω, excess amount of heat is generated leading to rapid diffusion between Al and Cu resulting in the formation of *Kirkendall voids*. At lower ω, Cu rich IMCs are formed because of lesser diffusion of Cu in Al. The Cu rich IMC like Al_4Cu_9 and $AlCu_4$ are the charge carriers and are

responsible for a continuous flow of current across the weld zone. The Cu exhibits pitting corrosion in the electrolytic medium which is due to presence of F in the electrolyte. The welded samples show higher corrosive resistance due to the formation of IMC. In the case of an electrolytic medium, with increasing ω, there is an increase in the corrosive nature and with increasing v, a change in the corrosion behaviour from anodic to cathodic has been observed. The Cu-rich IMCs are found to be harder and exhibiting better corrosion resistance. In the future, this study can further be extended by the dynamic stress analysis of the welded samples to determine their sustainability with varying conditions such as during deflections, vibrations, etc.

ACKNOWLEDGMENTS

The authors are grateful to Hall Effect Lab of the Physics Department and EPP lab of the Mechanical Engineering Department at IIT Kharagpur for providing the facilities to carry out the post-weld studies.

REFERENCES

1. A. Eftekhari, *ACS Sustain. Chem. Eng.* 7, 3684 (2018). https://doi.org/10.1021/acssuschemeng.7b04330.
2. C. Iclodean, B. Varga, N. Burnete, D. Cimerdean, and B. Jurchiş, *IOP Conf. Ser. Mater. Sci. Eng.* 252, 012058 (2017). https://doi.org/10.1088/1757-899x/252/1/012058.
3. S. Shawn Lee, T.H. Kim, S.J. Hu, W.W. Cai, and J.A. Abell, in *MSEC2010-34168* (2015). https://doi.org/10.1115/msec2010-34168.
4. P. Wolfram, N. Lutsey, ICCT (2016), pp. 1–23. https://doi.org/10.13140/rg.2.1.2045.3364.
5. H.K. Charles, *Appl. Phys. Lab.* 26, 402 (2005).
6. V.V. Silberschmidt, *Advanced Materials Modelling for Structures. Advanced Structured Materials*, ed. H. Altenbach and S. Kruch (Berlin: Springer, 2013), p. 307.. https://doi.org/10.1007/978-3-642-35167-9.
7. G.L.B. Matijasevic and L. Brandt, *Electr. Eng.* II, 17 (2009).
8. A. Das, L. Dezhi, W. David, and G. David, *World Electr. Veh. J.* 9, 1 (2018). https://doi.org/10.3390/wevj9020022.
9. D. Nagy and O. Krammer, *Solder. Surf. Mt. Technol.* (2017). https://doi.org/10.1108/SSMT-11-2016-0029.
10. M.J. Brand, E.I. Kolp, P. Berg, T. Bach, P. Schmidt, and A. Jossen, *J. Energy Storage* 12, 45 (2017). https://doi.org/10.1016/j.est.2017.03.019.
11. J. Hayashi and Y. Miyazawa, *IJST-2013 IOP Conf Ser. Mater. Sci. Eng.* (2014). https://doi.org/10.1088/1757-899x/61/1/012015.
12. P. Kah, R. Suoranta, and J. Martikainen, in *Proceedings of 16th International Conference on Mechanika* (2011). https://doi.org/10.13140/2.1.3298.1284.
13. J. Huang, X. He, Y. Guo, Z. Zhang, Y. Shi, and D. Fan, *J. Manuf. Process.* 25, 16 (2017). https://doi.org/10.1016/j.jmapro.2016.10.003.
14. S. Ukita, K. Kokubo, T. Masuko, and T. Irie, *Weld. Int.* 17, 541 (2003). https://doi.org/10.1533/wint.2003.3143.
15. R. Borrisutthekul, P. Mitsomwang, S. Rattanachan, and Y.M. Mutoh, *Energy Res J* 1, 82 (2010).
16. G. Chryssolouris, *Mech. Eng. Ser* (2003). https://doi.org/10.1007/978-1-4757-4084-4.
17. I. Mys and M. Schmidt, *Proc. SPIE* 6107, 610703 (2006). https://doi.org/10.1117/12.648376.
18. T. Solchenbach, P. Plapper, and W. Cai, *J. Manuf. Process.* 16, 183 (2014). https://doi.org/10.1016/j.jmapro.2013.12.002.
19. W. Thomas and E. Nicholas, *Mater. Des.* 18, 269 (1997). https://doi.org/10.1016/S0261-3069(97)00062-9.
20. D. Mishra, S.K. Sahu, R.P. Mahto, S.K. Pal, and K. Pal, *Lect. Notes Multidiscip. Ind. Eng.* (2019). https://doi.org/10.1007/978-981-13-0378-4_6.
21. M.P. Iqbal, R. Jain, and S.K. Pal, *J. Mater. Process. Technol.* 274, 116258 (2019). https://doi.org/10.1016/j.jmatprotec.2019.116258.
22. D. Mishra, R.B. Roy, S. Dutta, S.K. Pal, and D. Chakravarty, *J. Manuf. Process.* 36, 373 (2018). https://doi.org/10.1016/j.jmapro.2018.10.016.
23. R.P. Mahto, R. Kumar, S.K. Pal, and S.K. Panda, *J. Manuf. Process.* 31, 624 (2018). https://doi.org/10.1016/j.jmapro.2017.12.017.
24. R.P. Mahto, C. Gupta, M. Kinjawadekar, A. Meena, and S.K. Pal, *J. Manuf. Process.* 38, 370 (2019). https://doi.org/10.1016/j.jmapro.2019.01.028.
25. K.P. Mehta and V.J. Badheka, *Mater. Manuf. Process.* 31, 233 (2016). https://doi.org/10.1080/10426914.2015.1025971.
26. O. Mypati, A. Sadhu, S. Sahu, and D. Mishra, *J. Eng. Manuf.* (2019). https://doi.org/10.1177/0954405419838379.
27. R.P. Mahto, R. Bhoje, S.K. Pal, H.S. Joshi, and S. Das, *Mater. Sci. Eng. A* 652, 136 (2016). https://doi.org/10.1016/j.msea.2015.11.064.
28. R.P. Mahto and S.K. Pal, in *MSEC*, vol 1 (2018).
29. R. Beygi, M. Kazeminezhad, and A.H. Kokabi, *Trans. Nonferrous Metals Soc. China* 22, 2925 (2012). https://doi.org/10.1016/s1003-6326(11)61555-0.
30. A. Elrefaey, M. Takahashi, and K. Ikeuchi, *J. High Temp. Soc.* 30, 286 (2004).
31. I. Galvão, J. Oliveira, A. Loureiro, and D. Rodrigues, *Sci. Technol. Weld. Join.* 16, 681 (2011). https://doi.org/10.1179/1362171811Y.0000000057.
32. I. Galvão, C. Leitão, A. Loureiro, and D.M. Rodrigues, *Mater. Des.* 42, 259 (2012). https://doi.org/10.1016/j.matdes.2012.05.058.
33. A. Elrefaey, M. Takahashi, and K. Ikeuchi, *Weld. World* 49, 93 (2005). https://doi.org/10.1007/BF03266481.
34. I. Galvão, D. Verdera, D. Gesto, A. Loureiro, and D.M. Rodrigues, *J. Mater. Process. Technol.* 213, 1920 (2013). https://doi.org/10.1016/j.jmatprotec.2013.05.004.
35. P. Kah, C. Vimalraj, J. Martikainen, and R. Suoranta, *Int. J. Mech. Mater. Eng.* (2015). https://doi.org/10.1186/s40712-015-0037-8.
36. S. Sattari, H. Bisadi, and M. Sajed, *Int. J. Mech. Appl.* 2, 1 (2012). https://doi.org/10.5923/j.mechanics.20120201.01.
37. S. Ahmed, A. Shubhrant, A. Deep, P. Saha, in *AIMTDR* (2014), pp. 1–5.
38. D. Kim, J.H. Chang, J. Park, and J.J. Pak, *J. Mater. Sci. Mater. Electron.* 22, 703 (2011). https://doi.org/10.1007/s10854-011-0357-2.
39. M. Elsa, A. Khorram, O.O. Ojo, and M. Paidar, *Acad. Proc. Eng. Sci.* (2019). https://doi.org/10.1007/s12046-019-1103-3.
40. K. Hiroshi and O. Seiichi, *Trans. JIM* 11, 431 (1970).
41. M.J.M. Hermans and M.H. Biglari, *The ELFNET Book on Failure Mechanisms, Testing Methods, and Quality Issues of Lead-Free Solder Interconnects* (Berlin: Springer, 2011)https://doi.org/10.1007/978-0-85729-236-0.
42. L. Valdes, *Proc. I-R-E* 29, 1429 (1952).
43. Y. Singh, *Int. J. Mod. Phys. Conf. Ser.* 22, 745 (2013). https://doi.org/10.1142/S2010194513010970.
44. N. Bowler and Y. Huang, *Meas. Sci. Technol.* (2005). https://doi.org/10.1088/0957-0233/16/11/009.
45. M.F. Goes, M.A. Sinhoreti, S. Consani, and M.A. Silva, *Braz. Dent. J. IOP Conf. Ser. Mater. Sci. Eng.* 9, 3 (1998). https://doi.org/10.1088/1742-6596/755/1/011001.
46. O. Mypati, S.K. Pal, and P. Srirangam, *TMS 2019 148th Annual Meeting & Exhibition Supplemental Proceedings* (Berlin: Springer, 2019)https://doi.org/10.1007/978-3-030-05861-6.
47. H. Abe, Hitachi chemical technical report, 54, 31.
48. S. Dai, J. Chen, Y. Ren, Z. Liu, and J. Chen, *Int. J. Electrochem. Sci.* 12, 10589 (2017). https://doi.org/10.20964/2017.11.28.

49. X. Zhang, B. Winget, M. Doeff, J.W. Evans, and T.M. Devine, *J. Electrochem. Soc.* (2005). https://doi.org/10.1149/1.2041867.
50. R.P. Mahto, S. Anishetty, A. Sarkar, O. Mypati, S.K. Pal, and J.D. Majumdar, *Mater. Metals Mater. Int.* (2018). https://doi.org/10.1007/s12540-018-00222-x.
51. R. Drevet, O. Aaboubi, and H. Benhayoune, *J. Solid State Electrochem.* (2012). https://doi.org/10.1007/s10008-012-1742-3.
52. R. Chakraborty, V.S. Seesala, S. Sengupta, S. Dhara, P. Saha, and K. Das, *Surf. Interfaces* 10, 1 (2018). https://doi.org/10.1016/j.surfin.2017.11.002.
53. S.V. Hainsworth, H. Chandler, and T. Page, *J. Mater. Res.* 11, 1987 (1996).
54. S. Weng, Y. Huang, F. Xuan, and L. Luo, *Proc. Eng.* 130, 1761 (2015). https://doi.org/10.1016/j.proeng.2015.12.325.